

Design, fabrication and demonstration of a MEMS steam generator for ejector pump applications

This article has been downloaded from IOPscience. Please scroll down to see the full text article.

2010 J. Micromech. Microeng. 20 104007

(<http://iopscience.iop.org/0960-1317/20/10/104007>)

View [the table of contents for this issue](#), or go to the [journal homepage](#) for more

Download details:

IP Address: 18.62.12.44

The article was downloaded on 15/09/2010 at 23:50

Please note that [terms and conditions apply](#).

Design, fabrication and demonstration of a MEMS steam generator for ejector pump applications

Feras Eid¹, Luis Fernando Velásquez-García² and Carol Livermore¹

¹ Department of Mechanical Engineering, MIT, 77 Mass. Ave., Cambridge, MA 02139, USA

² Microsystems Technology Laboratory, MIT, 77 Mass. Ave., Cambridge, MA 02139, USA

E-mail: feraseid@mit.edu, livermor@mit.edu and lfvelasq@mit.edu

Received 26 February 2010, in final form 28 April 2010

Published 14 September 2010

Online at stacks.iop.org/JMM/20/104007

Abstract

The design, fabrication, successful demonstration and characterization of a microfabricated steam generator based on the homogeneous catalytic decomposition of hydrogen peroxide are presented. The device consists of a mixer, a reactor and a nozzle, and it produces a jet of high-speed steam that can be used for driving ejector pumps and for nanosatellite microthrusters. Numerically implemented coupled chemical, thermal and fluidic modeling was used to design the device, which was then fabricated via bulk micromachining and enclosed in a thermally insulating package. The device operated successfully with 90% peroxide catalyzed by a ferrous chloride tetrahydrate solution. Refractive index analysis is used to confirm full peroxide decomposition, and visual inspection and temperature measurements are used to confirm full water vaporization. The experimental results are analyzed to provide comprehensive model verification.

(Some figures in this article are in colour only in the electronic version)

1. Introduction

MEMS ejector pumps offer a promising approach to microscale gas pumping for moderate pressure rises [1]. Compared with existing MEMS gas pumps, ejector pumps offer much higher flow rates, along with robust operation and no moving parts. In an ejector pump, a high-speed gas stream (the motive flow) entrains and mixes with a low-speed stream (the suction flow). The suction fluid is pumped via the conversion of part of the mixed flow's kinetic energy into pressure rise. Steam chemically generated from a liquid precursor is often used for the motive fluid source since it offers significant advantages over compressed air (which needs a reservoir with a large volume) and over steam generated by vaporizing a water reservoir (which requires an external heat source and has a slow response).

A liquid precursor from which steam will be generated must meet certain requirements. First, it must have a high energy content in order to ensure a completely gas-phase device output. Second, it should be sufficiently safe and environmentally-friendly for its intended application.

Aqueous high-test hydrogen peroxide is a promising candidate for the chemical generation of steam to drive ejector pumps. In addition to having a high stored energy density, it is also environmentally-friendly and nontoxic when compared to other liquids, such as hydrazine, that were historically used for high-speed gas generation. Hydrogen peroxide decomposes catalytically to produce oxygen gas, water and heat that subsequently vaporizes the water. A microscale device that generates steam via this approach can thus be integrated into a MEMS ejector pump to provide the motive fluid. High-speed flow mixing analysis using the conservation of mass, momentum and total energy shows that by decomposing $17.5 \times 10^{-5} \text{ kg s}^{-1}$ of peroxide, such a device is capable of driving a two-stage ejector pump at a flow rate per unit of pump volume of about $10^{-2} \text{ g s}^{-1} \text{ cm}^{-3}$, which is at least two orders of magnitude higher than the capacity of state-of-the-art MEMS gas pumps [2–4]. Closely related devices can also be used as monopropellant microthrusters for impulse maneuvers in nanosatellites [5].

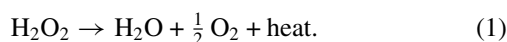
To the authors' knowledge, previous attempts at demonstrating microscale steam generators based on the above

approach have generally been unsuccessful [5, 6], although peroxide decomposition has been successfully reported in macromachined mesoscale devices operated at a high supply pressure, as in [7] where the reactor volume and supply pressure were at least 78 times and 7.5 times of their values in the current work, respectively. One of the challenges with microscale devices is that, as the size is reduced, the ratio of the surface area to volume increases. Therefore, the heat losses become significant compared to the heat generated by the exothermic reaction inside the device, and the energy remaining inside may not be sufficient for sustaining the reaction and vaporizing the water produced. The effects of boundary layers also become more pronounced at small scales and can lead to significant deviations from inviscid behavior. Finally, prior devices have typically used a heterogeneous catalyst coated on the device walls, which necessitates very narrow flow channels to maximize the reaction surface area; this can make the device prone to clogging. Such a static catalyst layer is also susceptible to poisoning by stabilized peroxide and eventually becoming ineffective.

In the current work, the above challenges are addressed by using multi-domain physical modeling to simulate the reacting flow and evaluate the heat losses from the device. The results guide the design of both a MEMS device that decomposes hydrogen peroxide using a homogeneous catalyst and a package with sufficiently high thermal resistance to enable full peroxide decomposition and complete water vaporization. The model includes the effects of boundary layers in the flow; these effects are compensated for in the design. Finally, by using a continually supplied homogeneous liquid catalyst, the poisoning problem of heterogeneous catalysts is eliminated, at the expense of adding a mixer section for the peroxide and catalyst streams.

2. Concept, modeling and design

Steam is generated from the decomposition of hydrogen peroxide according to the chemical reaction:



The decomposition is facilitated by a homogeneous catalyst solution that is mixed with the peroxide inside the device. The above exothermic reaction first produces liquid water, which is then vaporized by the heat generated. The gaseous products are subsequently accelerated to the required speed. To allow these functionalities, the device consists of three sections: a mixer, a reactor and a nozzle. A schematic of the overall device is shown in figure 1, and the models that were used to design the different sections are described below. Even though these models for the mixer, reactor, nozzle and thermal management are presented sequentially, they are in fact interdependent and iteration is required between them to arrive at the final design.

2.1. Mixer

The mixer is designed to achieve thorough mixing of the peroxide and catalyst streams before the flow enters the reactor,

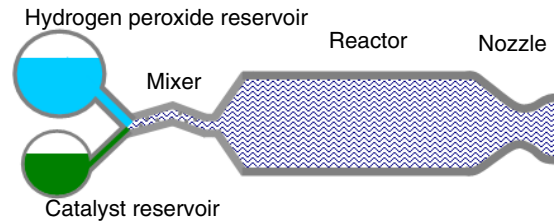


Figure 1. Schematic of the device.

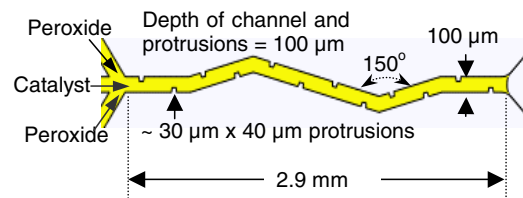


Figure 2. Mixer design.

while keeping the device compact and also ensuring that the supply pressure is kept below 5 atm to prevent package failure. Four mixers are used in parallel to minimize the pressure drop across the device. Each mixer consists of a narrow zigzag channel with protrusions on the walls. The inlet to each channel has three branches: a catalyst branch sandwiched between two peroxide branches. The mixer design is shown in figure 2.

A typical challenge in micromixing is the laminar nature of microflows, which makes diffusion dominant and mixing slow. Chaotic mixing can be established by using three-dimensional designs; this increases the mixing rate at the expense of significantly complicating the fabrication process. Two-dimensional static micromixers are chosen for their straightforward fabrication and their potential for rapid mixing in certain flow regimes. Engler *et al* [8] have shown that these devices have three flow regimes with different mixing speeds. These regimes are distinguished by a dimensionless identification number K which is different from the hydraulic-diameter-based Reynolds number that is typically used for identifying the nature of macroscale internal flows. This identification number K is equal to the ratio of the channel's hydraulic diameter d_h to the Kolmogorov length scale λ_k , which is the scale of the smallest eddies in a turbulent flow:

$$K = d_h / \lambda_k. \quad (2)$$

Conceptually, K is a measure of the free space for growth of vortices. At low values of K , the fluid viscosity damps the starting of eddies and mixing is slow, whereas at higher K values, the flow conditions allow for the formation and growth of eddies and vortices which enhance mixing. Engler *et al* have found in experiments and simulations that the critical value of K is about 45. When K exceeds this critical value, the flow in the mixer starts to have instabilities, and streamlines from each species start reaching into the opposite half of the channel in a swirling manner. This 'engulfment flow' regime exhibits faster mixing than any other micromixer flow regime, with mixing times on the order of a few milliseconds being observed in [8]. Mixing at the millisecond time scale is important in the

current work because it minimizes the mixer length and enables a compact device. Using the definition of λ_k and following the derivation in [8], K can be expressed as

$$K = \left(\frac{\Delta P}{\rho V^2} \frac{d_h}{L_v} Re^3 \right)^{\frac{1}{4}}. \quad (3)$$

In (3), L_v is the volume-to-area ratio of a control volume encompassing the mixer inlet region (as defined in [8]) and is equal to about six times the mixer channel width in our case. ΔP is the pressure drop in this control volume, ρ is the flow density, V is the flow velocity, d_h is the channel's hydraulic diameter and Re is the Reynolds number based on d_h . Note that V and Re can be found from the mass flow rate, the channel geometry and the flow density and viscosity, and ΔP can be estimated to first order using the Hagen–Poiseuille equation. K can then be expressed as

$$K = \left(32 \frac{L_i}{L_v} Re^2 \right)^{\frac{1}{4}}. \quad (4)$$

In (4), L_i is the equivalent mixer inlet length (following [8]) and is found to be about four times the mixer channel width (or 67% of L_v) for our case.

Using this analysis, the current mixer is designed to achieve K of about 48, ensuring engulfment flow and a residence time of around 1 ms, ensuring good mixing based on the results of Engler *et al*. Two extra features are added to the design: wall protrusions and zigzag channels. These have been shown by [9] and [10] respectively to significantly enhance mixing compared to a straight channel with smooth walls. With this design, the total mixer pressure drop is estimated to be about 2 atm, which keeps the required supply pressure less than 5 atm for the intended reactor pressures.

2.2. Reactor

The reactor is designed to achieve complete peroxide decomposition and full water vaporization. In the reactor, the peroxide decomposes according to (1). The flow in the reactor passes through five stages based on the thermodynamic phases of the species present. In stage 1, liquid peroxide decomposes into liquid water and oxygen gas, and the heat released causes the reactor temperature to rise. Once the boiling temperature of water at the reactor pressure is reached, stage 2 commences, in which water starts vaporizing at constant temperature. Once all the water has been vaporized, stage 3 begins, in which the liquid peroxide decomposes to produce steam and oxygen gas, and the heat released again causes the temperature to increase. This continues until the boiling point of the peroxide at the reactor pressure is reached and stage 4 begins. In stage 4, the peroxide changes phase at constant temperature. Once all of the peroxide has been vaporized, stage 5 starts and continues until all the peroxide has decomposed.

To study the flow in the reactor, some approximations are made to allow numerical modeling with reasonable time and computational effort. First, the models are limited to steady-state behavior, and the experimental conditions are chosen so that the timescale of the transient effects is only a small fraction of each experimental run. A bulk one-dimensional model is

Table 1. Variation of state variables during different reactor stages.

	Stage 1	Stage 2	Stage 3	Stage 4	Stage 5
Y_P	dec	dec	dec	dec	dec
T	inc	$T_{b,W}$	inc	$T_{b,P}$	inc
f_W	0	inc	1	1	1
f_P	0	0	0	inc	1
Start	$x = 0$	$T = T_{b,W}$	$f_W = 1$	$T = T_{b,P}$	$f_P = 1$
End	$T = T_{b,W}$	$f_W = 1$	$T = T_{b,P}$	$f_P = 1$	$Y_P = 0$

used, which is roughly justified by the reactor length being approximately 4.4 times its hydraulic diameter. Finally, the pressure inside the reactor is assumed to be constant since the pressure losses in the device are dominated by those occurring in the much narrower mixer channels. Pressure losses due to the phase change in the reactor are approximated and found to be negligible compared to the total pressure at the reactor inlet. With these assumptions, a state-space model is constructed in MATLAB where the state or independent variables are taken to be the flow temperature T , the peroxide mass fraction Y_P and the peroxide and water qualities, f_P and f_W , respectively. The quality of a two-phase (liquid–gas) species is the mass of that species in the gas phase divided by the total mass of the species present. Table 1 describes the variation of each state variable during the different stages (inc = increasing, dec = decreasing and $T_{b,W}$ and $T_{b,P}$ are the boiling points of water and peroxide, respectively, at the reactor pressure). The last two rows of this table show the criteria used by the program to determine the beginning and end of each stage; the stages are traversed sequentially.

To study the evolution of the state variables versus distance x along the reactor flow length (which is equivalent to time under steady-state conditions), the numerical program divides the reactor into lengthwise differential elements and applies conservation of mass, conservation of energy and species transport principles to each element while accounting for the chemical reaction within each element and the heat loss from the walls. With some algebraic manipulation, these laws can be combined and expressed in the following state-space form. (Note that in (6), two of the three terms on the left-hand side vanish for each stage.)

$$dY_P/dx = -M_P R_r A / \dot{m}, \quad (5)$$

$$\begin{aligned} \dot{m} \bar{c}_p dT/dx + \dot{m} Y_P h_{fg,P} df_P/dx + \dot{m} Y_W h_{fg,W} df_W/dx \\ = -\Delta H_R R_r A - dQ_{\text{loss}}/dx. \end{aligned} \quad (6)$$

In the above equations, M_P is the molar mass of peroxide, R_r is the reaction rate, A is the reactor cross-sectional area, \dot{m} is the total mass flow rate, \bar{c}_p is the average (mass-weighted) specific heat of the flow, $h_{fg,P}$ and $h_{fg,W}$ are the enthalpies of vaporization of the peroxide and water, respectively, ΔH_R is the heat of reaction (negative for an exothermic reaction) and Q_{loss} is the rate of heat loss from the reactor walls, which is discussed in detail in section 2.4. The quantities \bar{c}_p , $h_{fg,P}$, $h_{fg,W}$, and ΔH_R are expressed as functions of temperature using empirical property relationships [11]. The reaction rate is the number of moles of peroxide reacting per unit time and unit reactor volume and is given by

$$R_r = k_P Y_P / M_P. \quad (7)$$

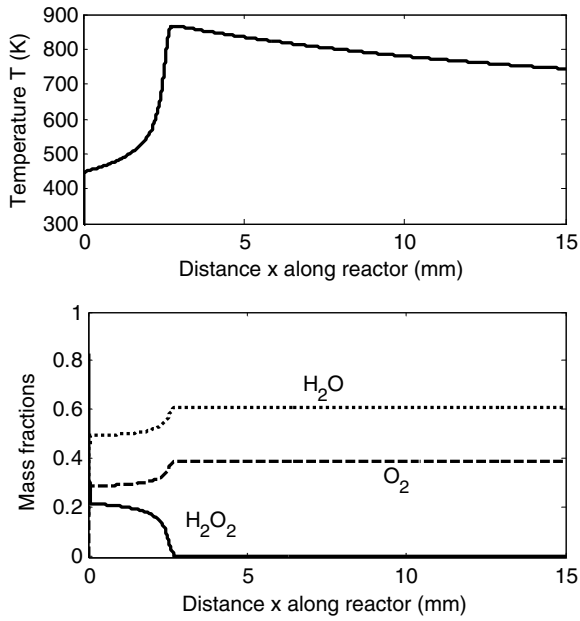


Figure 3. Plot of flow temperature (top) and species' mass fractions (bottom) versus distance along the reactor.

In (7) k is the reaction rate constant, empirically given by [12, 13]

$$k = 10^5 \quad (\text{Stages 1-4})$$

$$k = 10^9 \exp[-54800/(R_u T)] \quad (\text{Stage 5}), \quad (8)$$

where R_u is the universal gas constant.

The above equations (5) and (6) are solved simultaneously in MATLAB using an ODE solver capable of handling stiff differential equations. Once the state variables are evaluated, all other related flow parameters can be estimated using either constitutive relations (e.g. equations of state), the conservation of mass, or stoichiometry.

Using the above model, the reactor is designed to be a 15 mm long rectangular chamber with a 4 mm × 3 mm cross section. The flow temperature and species' mass fractions predicted by the model are plotted versus distance along the reactor in figure 3, for the case of a 90% HTP mixture supplied at 7.0 mL min⁻¹ and catalyzed by a ferrous chloride tetrahydrate solution (80% saturated) at 0.5 mL min⁻¹, which corresponds to an overall initial peroxide mass fraction of 83% (after mixing with the catalyst). These are the design conditions at which the device performance is predicted to be optimized. In addition to simulating the design conditions, the numerical program above is expanded to study the device operation over a range of overall initial peroxide mass fractions between 71% and 83%. The minimum overall initial peroxide mass fraction required for full peroxide decomposition with this device and package design was found to be about 74%, as discussed in section 4. The results of this parametric study are then verified experimentally to assess the accuracy of the model, as described in section 4.3. The predicted reactor pressure is always less than about 2 atm.

2.3. Nozzle

The nozzle is designed to eject the flow from the reactor chamber to the atmosphere, thereby expanding the flow and reducing its pressure. The nozzle has two sections: a converging section where the flow is accelerated to sonic velocity and a diverging section where the flow becomes supersonic. First, an isentropic one-dimensional compressible flow model is used to approximate the dimensions of the throat and exit sections, and then the design is refined by accounting for heat loss and boundary layer formation. The nozzle depth is kept the same as that of the reactor (3 mm) to simplify the device fabrication.

At any location along the nozzle, the Mach number can be determined from the flow velocity V and temperature T , using

$$M = V/\sqrt{\gamma RT}. \quad (9)$$

In (9), γ and R are, respectively, the specific heat ratio and mass-based gas constant of the flow in the nozzle, which is assumed to be composed of oxygen and steam in concentrations determined from the reactor model. Using (9) to estimate the Mach number M_i at the nozzle inlet (i.e. reactor exit) of known area A_i and assuming the flow to be sonic ($M_t = 1$) at the throat, the isentropic M - A relation is then applied between the inlet section (subscript 1) and throat section (subscript 2) to calculate the throat area A_t :

$$A_1 \frac{M_1}{\left(1 + \frac{\gamma-1}{2} M_1^2\right)^{\frac{0.5(\gamma+1)}{\gamma-1}}} = A_2 \frac{M_2}{\left(1 + \frac{\gamma-1}{2} M_2^2\right)^{\frac{0.5(\gamma+1)}{\gamma-1}}}. \quad (10)$$

To determine the nozzle exit area A_e , the exit Mach number M_e is first calculated by applying the M - P isentropic relation between the inlet and exit sections of the nozzle:

$$\frac{P_i}{P_e} = \left(\frac{1 + \frac{\gamma-1}{2} M_e^2}{1 + \frac{\gamma-1}{2} M_i^2}\right)^{\frac{\gamma}{\gamma-1}}. \quad (11)$$

In (11), P_i is the known inlet pressure (i.e. reactor pressure) and P_e is the exit pressure which is deliberately matched to that of the atmosphere in this case to prevent the formation of shock or expansion waves at the nozzle exit. Then, the isentropic M - A relation (10) is applied again in order to calculate A_e , this time taking the inlet to be section 1 and the exit to be section 2.

The nozzle length is set somewhat arbitrarily at 2.3 mm by trying to minimize the overall device volume without causing strongly non-ideal flow behavior, such as separation from the nozzle walls. The isentropic flow assumption is then relaxed, and the variations of the flow Mach number M , stagnation temperature T_t and stagnation pressure P_t with distance x along the nozzle are determined by using the following compressible flow model [14] that accounts for heat loss from the nozzle walls but assumes constant flow molecular weight and specific heats:

$$\dot{m} \bar{c}_p dT_t/dx = -dQ_{\text{loss}}/dx, \quad (12)$$

$$\frac{dM^2}{dx} = \frac{M^2}{1 - M^2} \left(1 + \frac{\gamma - 1}{2} M^2\right) \times \left(-\frac{2}{A} \frac{dA}{dx} + \frac{1 + \gamma M^2}{T_t} \frac{dT_t}{dx}\right), \quad (13)$$

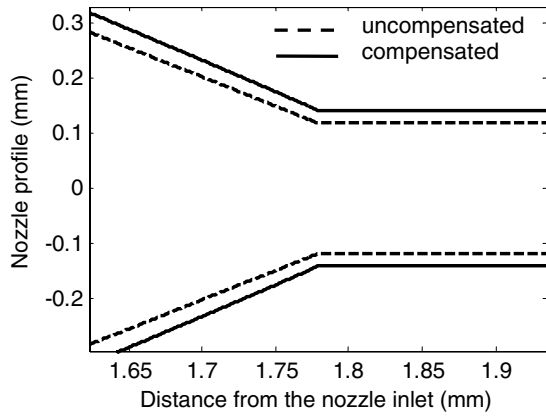


Figure 4. Plot of the nozzle profile near throat, before and after boundary layer compensation.

$$\frac{dP_t}{dx} = -\frac{\gamma M^2 P_t}{2T_t} \frac{dT_t}{dx} \quad (14)$$

The above equations (12)–(14) are solved simultaneously in MATLAB using an ODE solver. The static flow temperature T and pressure P at any x can then be determined from the static-stagnation property relations.

The flow density can then be calculated using the ideal gas law and the flow velocity V from mass conservation or (9). These parameters and the flow viscosity μ (which is an empirically determined function of temperature [11]) are then used to estimate the thickness of boundary layers in the nozzle. These layers tend to lower the mass flow rate from its ideal (frictionless) value, and their effect is most pronounced near the nozzle throat where they could prevent the design from achieving sonic (and subsequently supersonic) conditions unless accounted for. The displacement thickness δ^* is selected as the measure of the boundary layer thickness and is evaluated following the Blasius solution [15]. The displacement thickness is defined as the distance by which the walls in a boundary layer flow would have to be pulled apart to maintain the same mass flow rate as a hypothetical frictionless flow with the same density and initial wall separation, and it is calculated using

$$\delta^* = 2 \times 1.72 \sqrt{\mu x / (\rho V)}. \quad (15)$$

The factor of 2 in (15) accounts for the formation of boundary layers on both sidewalls of the nozzle; the effect of top and bottom wall boundary layers is less critical since the nozzle width is much smaller than its depth near the throat. Thus, the nozzle width is increased by δ^* to leave the mass flow rate unaltered. Figure 4 plots the nozzle design near the throat before and after boundary layer compensation. Note that the actual fabricated design replaces the sharp corners at the throat with filleted ones to lower the frictional losses. The nozzles of the fabricated devices have a throat width of approximately 236 μm .

2.4. Thermal management

Thermal management is key to ensuring successful operation of the device. As can be seen from the right-hand side of

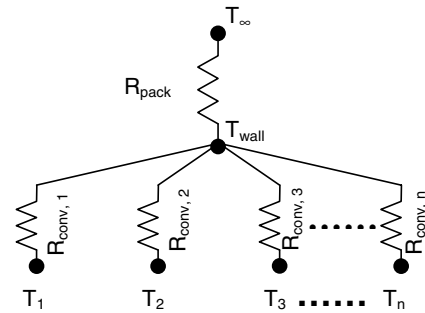


Figure 5. Thermal network between the device and environment at the steady state.

(6), there is competition between the heat generation inside the device and the heat loss from the walls. Without proper management, the heat loss term dQ_{loss}/dx can prevent the temperature from rising to the desired values. This can lead to incomplete water vaporization, as well as causing incomplete peroxide decomposition by slowing down the temperature-dependent reaction rate constant in stage 5, given by (8).

To minimize the heat losses, two packaging schemes are evaluated: suspending the device in air with fluidic connections made via long pipes adhered directly to the device surface (e.g. by epoxy) and encasing the device inside a machined package using O-rings and threaded fittings. In the first approach, the flow loses heat by internal forced convection to the device walls and then by external natural convection to the ambient air. This approach provides sufficient thermal insulation due to the low natural convection coefficient, but it is not selected because of robustness considerations. In the second and more robust approach, the flow loses heat by internal forced convection to the device walls and then by conduction through the package to the environment. This second approach is selected, and the reactor model is used to determine the minimum required thermal resistance of the package. First, the resistance due to conduction within the silicon walls is estimated and found to be very small compared to that due to the flow’s internal convection, thus justifying the assumption of isothermal device walls. Then, the thermal network shown in figure 5 is used to study heat transfer between the device and the environment at the steady state. Here, R_{pack} is the conduction thermal resistance of the package, $R_{\text{conv},m}$ is the convection thermal resistance in each differential reactor or nozzle element at average element temperature T_m and T_∞ is the ambient temperature.

Each differential convection resistance is given by

$$R_{\text{conv},m} = 1/(h_{\text{conv}} dA_{\text{surf}}), \quad (16)$$

where h_{conv} is the local convection coefficient found using empirical heat transfer correlations [16], and dA_{surf} is the differential surface area over which convection takes place. The heat loss from the flow at each node is thus given by

$$\frac{dQ_{\text{loss},m}}{dx} = \frac{d}{dx} \left(\frac{T_m - T_{\text{wall}}}{R_{\text{conv},m}} \right) = h_{\text{conv}} (T_m - T_{\text{wall}}) \frac{dA_{\text{surf}}}{dx}, \quad (17)$$

where T_{wall} is the wall temperature. The program finds T_{wall} by iteration, starting with a guess value to calculate the node



Figure 6. Machined package parts.

temperatures T_m and then using these to refine the value of T_{wall} by applying Kirchoff's current law:

$$\sum [(T_m - T_{wall})/R_{conv,m}] = (T_{wall} - T_{\infty})/R_{pack}. \quad (18)$$

This process is repeated until T_{wall} converges. Note that in (18) R_{pack} is not known yet, so different (decreasing) values are tried with the reactor and nozzle models to determine the minimum resistance that will allow complete peroxide decomposition and water vaporization, with no condensation in the nozzle. Once this minimum value is estimated, the package is designed to have a thermal resistance well above this value. For a given geometry, this criterion is used to determine the maximum package thermal conductivity k_{pack} , assuming that the outer package surfaces are at the ambient temperature and that the device surfaces that are directly exposed to air (see figure 6) are cooled by natural convection. For the final design of the device and package, the minimum value of R_{pack} to obtain full peroxide decomposition and product vaporization is 4 K W^{-1} . In addition to having a low thermal conductivity, the package material must also meet other requirements, such as having a melting point that is high enough to sustain the reactor temperatures reached, having sufficiently tight machining tolerances to allow successful installation of the O-rings, and being compatible with peroxide. Based on these considerations, the package was constructed from a mica-based ceramic composite (Rescor 914, from Cotronics Corp.). The package consists of the two parts shown in figure 6; these are clamped together using fasteners. The top part (left) has a slot in which the device sits and a window for optical access during the experiments. The bottom part (right) has holes for thermocouple insertion, O-ring glands, and threaded ports on the backside (not visible in the figure above) for connecting the peroxide and catalyst supplies.

3. Fabrication

The device consists of five bonded wafers, as shown in figure 7. Layers 1 through 4 are silicon wafers; layer 1 is about 0.5 mm thick and the rest are 1 mm thick. Layer 5 is a blank, 0.5 mm thick Pyrex wafer that caps the device and provides optical access.

Layer 1 contains the inlet holes for the peroxide and catalyst streams along with thermocouple insertion holes to measure the silicon wall temperature. It is fabricated using photolithography and deep reactive ion etching (DRIE). Layer 3 contains through holes and some of the reactor and

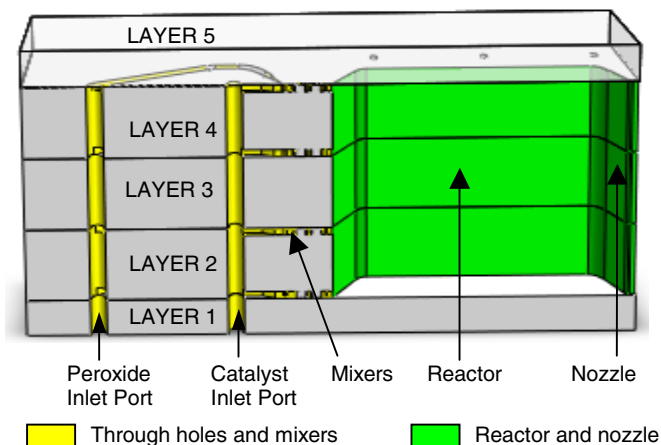


Figure 7. Schematic cross section of the device.

nozzle depths and is fabricated similarly to layer 1 while using an oxide layer as a hard mask in addition to the resist mask. Layers 2 and 4 are identical and contain the relatively shallow mixers on both sides of each layer in addition to the remaining deep-etched features. The different depths of the mixers and the deep features necessitate a 'nested mask' approach using a combination of photoresist and oxide layers as masks. The device's fabrication process flow is shown in figure 8. The four patterned silicon layers are then bonded together using silicon direct bonding, and the stack is anodically bonded to the Pyrex wafer and dicesawed. A microfabricated device is shown in figure 9.

4. Testing

4.1. Test rig setup

A schematic of the experimental setup is shown in figure 10. The experiments are run using high-test hydrogen peroxide purchased at 90% concentration (FMC Chemicals) and diluted as necessary, with ferrous chloride tetrahydrate as a catalyst (Sigma Aldrich). Syringe pumps (Chemyx Inc.) supply controlled volume and mass flow rates of both solutions. Pressure relief valves (Swagelok) prevent pressure buildup in the system. Pressure buildup is a hazard when working with a strong oxidizer such as peroxide and necessitates not only pressure relief valves but also provision for chemical containment and dilution as necessary. Plug (on/off) valves (Swagelok) either connect the streams to the package or disconnect and purge each stream out of the system separately. Check valves (Kinesis Inc.) prevent either stream from flowing into the piping of the other stream through the package at startup. Care is taken to ensure that all components are made of materials that are chemically compatible with peroxide (e.g. PTFE, PEEK, certain Viton grades and passivated stainless steel).

4.2. Experiments

The criteria used to define effective steam generation by the device are full peroxide decomposition and complete

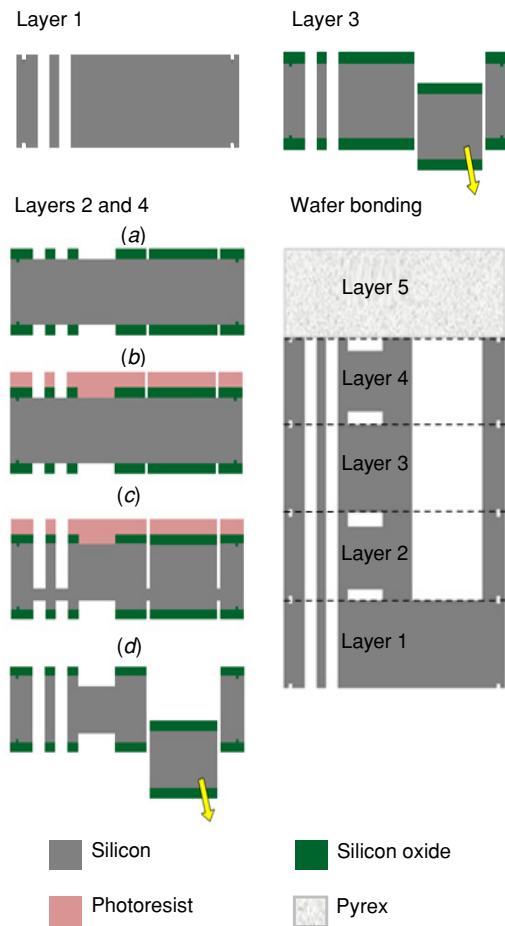


Figure 8. Fabrication process flow. Layer 1: deposit photoresist and pattern using photolithography. Etch silicon through using DRIE. Layer 3: deposit oxide to act as a hard mask. Deposit photoresist and pattern using photolithography. Etch oxide using RIE, and then etch silicon through using DRIE. Layers 2 and 4: (a) deposit oxide and photoresist on both sides. Pattern all features (deep and shallow) in photoresist using photolithography. Etch oxide using RIE. (b) Deposit photoresist on the top side and pattern deep features using photolithography. (c) Etch shallow features in bottom-side silicon using DRIE. Also using DRIE, etch all features in top-side silicon to a depth equal to the wafer thickness minus twice the shallow feature depth. (d) Remove photoresist and etch shallow features in top-side silicon using DRIE. Wafer bonding: remove all oxide from silicon wafers using HF dip. Fusion-bond the silicon wafers, and then anodically bond a Pyrex wafer to the silicon stack.

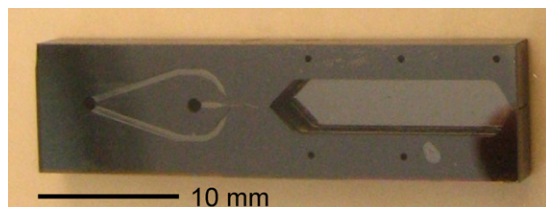


Figure 9. Photograph of a microfabricated device.

water vaporization. To test for these criteria and verify the model, experiments were run with three different initial HTP concentrations and flow rates as shown in table 2. The catalyst flow rate in all three experiments is fixed at

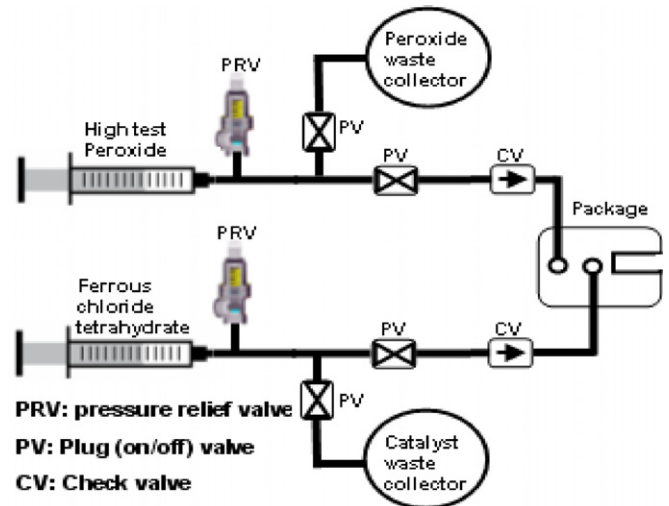


Figure 10. Schematic of the test rig setup.

Table 2. Peroxide flow rates and mass fractions during the three experiments.

	HTP stream flow rate (mL min ⁻¹)	Peroxide mass concentration in HTP stream (%)	Overall initial peroxide mass fraction after mixing with catalyst (%)
Exp 1	7.0	90.0	83
Exp 2	7.3	79.9	74
Exp 3	7.4	76.7	71

0.5 mL min⁻¹. Based on the model, the device is predicted to perform optimally at the conditions of experiment 1. The conditions in experiments 2 and 3 are predicted to bound the range of initial peroxide concentrations over which the peroxide decomposition inside the device changes from complete to incomplete. The peroxide concentrations and flow rates are chosen such that the total mass flow rate remains constant among all three experiments, which is necessary for successful sonic and supersonic acceleration of the flow in the nozzle. For experiments 2 and 3, 90% peroxide was diluted by adding DI water.

4.3. Characterization and analysis

The three experiments are characterized using refractometry and temperature measurements as described below. Experiment 1 is additionally characterized by visual inspection using a camcorder and lens system. These video records show that the device experiences three distinct temporal stages after the system is turned on. First, the device walls are cold, and a lot of liquid is emitted from the device, in addition to some gas. Then, the device walls start heating up, and all the liquid inside the device starts getting vaporized, but it condenses shortly upon exit since the temperature is still not high enough. Finally, the device walls reach the desired steady-state temperature dictated by the reaction, and the effluent is completely gaseous with no visible condensation near the exit. The first two stages last for about 30 s, and

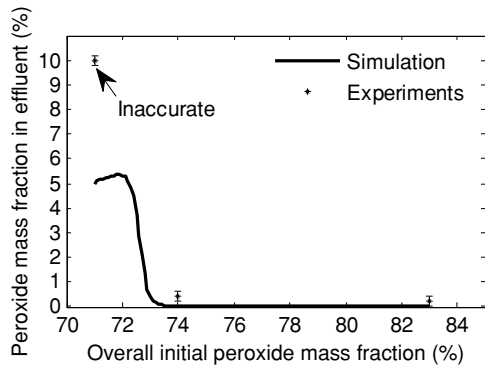


Figure 11. Plot of peroxide mass fraction in effluent from refractometry versus initial peroxide mass fraction.

the third (steady-state) stage extends for the remainder of the syringe pump cycle (about 11.5 min). This visual assessment serves as a first indicator of the complete vaporization of the effluent at the steady state, as predicted for the optimum conditions of experiment 1.

4.3.1. Refractometry. The effluent is captured in a clean cold glass beaker (at a distance where all the solid catalyst has fallen off due to gravity) and allowed to condense. Its refractive index is then measured using a hydrogen peroxide refractometer (Atago Co.) to determine the mass fraction of undecomposed peroxide at the exit. Figure 11 plots the model-predicted peroxide mass fractions in the effluent over a range of overall initial peroxide mass fractions between 71% and 83%, in addition to the experimentally measured effluent peroxide concentrations. The error in the refractometer reading is $\pm 0.2\%$. The model predicts that full peroxide decomposition will exist for overall initial peroxide mass fractions down to about 74%, below which some peroxide starts exiting the device undecomposed. Conceptually, this is due to the decreasing energy content of the HTP mixture as the peroxide concentration decreases, which causes the temperature-dependent reaction rate to slow down until the time spent by the flow inside the device is no longer enough to decompose all the peroxide. The theoretical curve is verified by the results of experiments 1 and 2, confirming successful device operation over the range of these two experiments. For experiment 3, the refractometer reading is about 10%, which confirms that decomposition is incomplete. This measurement, however, is significantly higher than the model prediction. This discrepancy is due to the limited capabilities of the refractometer, which is developed to analyze mixtures made exclusively of hydrogen peroxide and water. While this describes the effluent composition in experiments 1 and 2, it does not describe the situation in experiment 3. In experiment 3, there are additional intermediate species as well as dissolved catalyst in the two-phase effluent mixture, which is observed visually as well as predicted by the model to be liquid–gas for this case. Therefore, the refractometer reading for experiment 3 is considered to provide a qualitative rather than a quantitative indication of the undecomposed peroxide in the effluent.

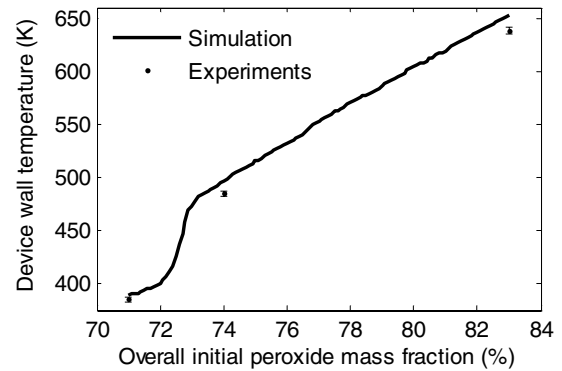


Figure 12. Plot of device wall temperatures versus initial peroxide mass fraction.

4.3.2. Temperature measurements. Thermocouples (Omega Engineering Inc.) are used to measure the temperatures of the effluent and the device walls. Figure 12 plots the model-predicted wall temperatures over the above range of overall initial peroxide mass fractions along with the experimental results. The error in the thermocouple readings is the greater of $\pm 2.2\text{ }^\circ\text{C}$ or $\pm 0.4\%$ of the measured value. The model shows that as the initial peroxide concentration is lowered, the wall temperature decreases linearly until incomplete peroxide decomposition starts, at which point there is a sharp nonlinear drop in wall temperature. The experimental results agree very well with the simulation.

The effluent temperatures are also measured experimentally and compared with the model. The theoretical quantity used for this comparison is the ‘adiabatic wall temperature’ T_{ad} of a solid placed at the same distance from the nozzle as the thermocouples. This adiabatic wall temperature [16] is the highest temperature that a solid placed in a heated high-speed flow can attain, and it provides a good estimate of the expected thermocouple reading. It is given by

$$T_{ad} = T + 0.5ru_{exp}^2/\bar{c}_p. \quad (19)$$

In (19), T is the static flow temperature at the nozzle exit, r is the recovery factor (found to be in the range of 0.94–1 from empirical correlations [16]) and u_{exp} is the flow velocity at the location of the thermocouple after free expansion in the atmosphere. This velocity can be determined from the predicted (pre-expansion) flow velocity at the nozzle exit and conservation of mass, using the experimental results of [17] to determine the extent of expansion, which depends on the location of the thermocouple as well as the nozzle dimensions at the exit. Table 3 shows the comparison of the predicted adiabatic wall temperature at the thermocouple location to the experimental measurements. The uncertainty in the experimental measurements (last column) is due to the error limits of the thermocouple wires used. The range in the predicted values for each experiment (first column) is due to the uncertainty in the exact thermocouple location (between 1 mm and 1.5 mm away from the nozzle exit) which affects the value of u_{exp} in (19). For the predicted values of experiment 3, there is an additional uncertainty in the quality of steam exiting since some condensation takes place in the nozzle. The steam quality affects r , u_{exp} and \bar{c}_p in (19), and the calculated range of

Table 3. Predicted and measured effluent temperatures.

	Predicted range in adiabatic wall temperature at thermocouple location (K)	Temperature measured by thermocouple (K)
Exp 1	623.1–643.4	623.0 ± 2.6
Exp 2	484.2–500.6	499.0 ± 2.2
Exp 3	354.9–375.8	360.0 ± 2.2

temperatures for this experiment corresponds to exit qualities between 20% and 80%. Two conclusions can be drawn from this table. First, the measurement in experiment 1 corresponds to a static temperature range of 562.9–583.2 K, which is well above the saturation temperature of steam under the given conditions (364.8 K), thus supplementing the visual inspection conclusion of complete water vaporization under the design conditions. Second, there is very good agreement between the predicted and experimental results, which provides further model verification.

5. Conclusions

In this paper, the design, fabrication, demonstration and characterization of a MEMS steam generator based on the catalytic decomposition of hydrogen peroxide have been reported. A multi-domain physical model is used to design the device and is then verified experimentally. Successful operation of the device, as witnessed by its ability to completely decompose the peroxide and fully vaporize the water produced, makes it very useful for driving MEMS ejector pumps after adjusting the nozzle to match the exit pressure to the upstream pumping pressure. The device can also be used as part of a nanosatellite monopropellant microthruster after adjusting the nozzle to produce a desired thrust level at a given specific impulse.

Acknowledgments

The authors thank Kimberlee Collins for the CFD simulation of the mixer. Microfabrication was carried out at the Microsystems Technology Laboratories (MTL) at MIT. This work was supported in part by the Tactical Technology Office

(Program Manager Dr Sheldon Meth) at the Defense Advanced Research Projects Agency (DARPA), in part by the Missile Defense Agency (MDA), and in part by the Air Force Research Laboratory through DARPA Order T171/00, Program Code: 4G10, issued by the DARPA Contracts Management Office under contract MDA972-04-C-0140. This work was also supported in part by the Microsystems Technology Office at DARPA (Program Manager Dr Dennis Polla) under Award W31P4Q-10-1-0005. The views and conclusions that are contained in this document are those of the authors and should not be interpreted as representing the official policies, either expressed or implied, of the DARPA or the US Government.

References

- [1] Chuech S G, Chen C C, Lu J C and Yan M M 2007 *Energy Convers. Manage.* **48** 2657–62
- [2] Kamper K P, Dopfer J, Ehrfeld W and Oberbeck S 1998 *Proc. MEMS 98* pp 432–7
- [3] Böhm S, Olthuis W and Bergveld P 1999 *Sensors Actuators A* **77** 223–8
- [4] McNamara S and Gianchandani Y 2005 *J. Microelectromech. Syst.* **14** 741–6
- [5] Hitt D L, Zakrzewski C M and Thomas M 2001 *Smart Mater. Struct.* **10** 1163–75
- [6] Osaki Y and Takahashi K 2004 *IEEE Trans. Sensors Micromachines* **123** 436–41
- [7] An S, Brahmī R, Kappenstein C and Kwon S 2009 *J. Propul. Power* **25** 1357–60
- [8] Engler M, Kockmann N, Kiefer T and Woias P 2004 *Chem. Eng. J.* **101** 315–22
- [9] Wong S H, Bryant P, Ward M and Wharton C 2003 *Sensors Actuators B* **95** 414–24
- [10] Mengeaud V, Josserand J and Girault H H 2002 *Anal. Chem.* **74** 4279–86
- [11] Yaws C L 1999 *Chemical Properties Handbook* (New York: McGraw-Hill)
- [12] Zhou X and Hitt D L 2003 *33rd AIAA Fluid Dynamics Conf. and Exhibition (Orlando, FL)*
- [13] Orr R J and Williams H L 1953 *J. Phys. Chem.* **57** 925–31
- [14] Greitzer E M, Tan C S and Graf M B 2004 *Internal Flow: Concepts and Applications* (New York: Cambridge University Press)
- [15] Kundu P K and Cohen I M 2004 *Fluid Mechanics* (San Diego, CA: Elsevier)
- [16] Mills A F 1999 *Heat Transfer* (Upper Saddle River, NJ: Prentice-Hall)
- [17] Quinn W R 1994 *AIAA J* **32** 547–54